Interpreting the single fiber fragmentation test with numerical simulations

van der Meer, Frans P.; Raijmaekers, Sibrand; Rocha, Iuri B.C.M.

DOI
10.1016/j.compositesa.2019.01.002

Publication date
2019

Document Version
Accepted author manuscript

Published in
Composites Part A: Applied Science and Manufacturing

Interpreting the single fiber fragmentation test with numerical simulations

Frans P. van der Meer[a,*], Sibrand Raijmaekers[b], Iuri B.C.M. Rocha[a,b]

[a] *Delft University of Technology, Faculty of Civil Engineering and Geosciences, PO Box 5048, 2600 GA Delft, The Netherlands*
[b] *Knowledge Centre WMC, Kluisgat 5, 1771 MV Wieringerwerf, The Netherlands*

Abstract

Characterization of the mechanical properties of the fiber/matrix interface is a challenge that needs to be addressed to enable accurate micromechanical modeling of failure in composite materials. In this paper a numerical investigation is presented into one of the tests that has been proposed for measuring these interfacial properties. A new cohesive zone model with friction is presented, as well as an original numerical framework for modeling of embedded fibers. The research generates new insight into the meaning of the single fiber fragmentation test, confirming the applicability of shear lag theory also in presence of multiple cracks, and emphasizing the relevance of matrix plasticity for the development of friction in the test. Although the frictional stress that can be obtained from the test should not be confused with the cohesive strength of the fiber/matrix interface, measurements of fracture process zone length can give indirect information on this cohesive strength.

Keywords: B. Interface/interphase; B. Mechanical properties; C. Computational modelling; C. Micro-mechanics

1. Introduction

Composite materials derive their advantageous properties from their microstructure. However, the inhomogeneity on the microlevel also makes it diffi-

*Corresponding author. Tel.: +31 15 278 5918
Email address: f.p.vandermeer@tudelft.nl (Frans P. van der Meer)

cult to predict their performance. To circumvent the need to formulate general phenomenological models for macroscopic composite material behavior, there is a drive towards micromechanical modeling, where the complex macroscopic material behavior follows from the behavior of the simpler constituents and their physical interaction. These micromechanical models need input on the behavior of fibers and resin, which can be measured from experiments on individual fibers or pure resin. However, for some applications, such as the modeling of failure, additional properties are needed for the fiber/matrix interface. These are much more difficult to obtain. Specifically, there is no consensus on how cohesive strength and fracture energy of the fiber matrix can be measured.

One of the tests that have been proposed for the characterization of the mechanical properties of the fiber/matrix interface is the Single Fiber Fragmentation Test (SFFT). This test involves axially loading a strip of resin with a single fiber embedded in its center. The test supposes that the fiber failure strain is significantly lower than the resin one. This leads to successive fiber break events followed by stress redistribution between fiber fragments through shear stresses in the resin and interface. The test proceeds until a saturation state when the distance between breaks is shorter than the one necessary to promote a new failure, the so-called critical length.

Starting from the classic work by Kelly and Tyson [1], numerous authors [2–5] have assumed the existence of an interface strength computed from the fiber strength and the critical length by supposing the existence of a constant shear stress along the entire length of the fiber. Since then, this simplifying assumption has been challenged by multiple authors for a number of reasons: Firstly, experimental measurements [6, 7] contradict the notion of a constant shear stress, even at higher strains. Secondly, the approach does not attempt to discern the relative roles of resin plasticity and interface friction and does not distinguish between intact and damaged interfaces [8, 9]. Thirdly, since the test often fails to reach a saturated state for a number of fiber/matrix combinations [10, 11], the main assumption of the simplified model is invalidated. The characterization of the interface through a single strength value, and the subse-

quent use of this value as input for numerical models, is therefore a questionable choice.

A number of authors have therefore sought to improve the material characterization capabilities of SFFT through a more realistic representation of the stress field along the fragmented fiber and the inclusion of additional failure modes. Nairn and Liu [12] developed an analytical model that describes the interface through a fracture energy and a friction parameter which was later used by Kim and Nairn [13] to analyze their experimental data. Later extensions by Tripathi et al. [14] and Johnson et al. [15] added the effects of residual stresses and matrix plasticity to the original model. Further analytical models were also developed by Wu et al. [16] and Hutchinson and Jensen [17] and more recently by Sørensen and Lilholt [18, 19] taking into account friction and residual stresses but neglecting the effects of matrix plasticity.

Comparatively fewer authors attempted to study the problem through numerical analysis. Varna et al. [20] developed an axisymmetric FE model of the SFFT considering residual stresses but assuming a linear-elastic behavior for the resin. Nishikawa et al. [10] included matrix plasticity and both interface debonding and matrix cracks in their FE model but neglected the effect of residual stresses and friction along the interface. Graciani et al. [11] opted for a model based on the Boundary Element Method (BEM) with residual stresses and friction but no plasticity. Therefore, no consensus seems to exist on which of these mechanisms should be included in a realistic numerical model of the fragmentation process and which intrinsic material properties may be discerned from the test.

In this paper, the single fiber fragmentation test is analyzed with two different numerical models. The aim of this research is to study whether simplifications in shear lag theory are justified. Shear lag theory assumes the presence of a constant friction, it neglects plasticity and it neglects interaction between different fiber/matrix debond cracks. For investigating the validity of these simplifications new model components have been developed: a new cohesive law with friction and a new finite element formulation for embedded fibers, sup-

porting breakage and debonding of these fibers.

2. Shear lag model

In this work we will make use of analytical expressions derived from a shear lag model by Sørensen [18, 19]. Sørensen's model assumes the presence of a constant frictional stress along the cracked fiber/matrix interface and a fracture process zone of negligible size with an associated fracture energy G_c. Under these assumptions the following relation exists between applied stress $\bar{\sigma}$ and debond length:

$$\frac{\bar{\sigma}}{E_\mathrm{c}} = \frac{\bar{\sigma}_\mathrm{i}}{E_\mathrm{c}} + \frac{2\tau l_\mathrm{d}}{E_\mathrm{f} r} \tag{1}$$

where E_c is the composite stiffness of the SFFT specimen (meaning that $\bar{\sigma}/E_\mathrm{c}$ is equal to the applied strain $\bar{\varepsilon}$), τ is the magnitude of the frictional stress, l_d is half the debond length, E_f is the fiber stiffness, r is the fiber diameter and $\bar{\sigma}_\mathrm{i}$ is the stress level at which debond length starts to grow (assuming the fiber break is already present). This crack growth stress level is related to the fracture energy G_c through:

$$\frac{G_c}{E_\mathrm{f} r} = \frac{1}{4}\left(\frac{\bar{\sigma}_\mathrm{i}}{E_\mathrm{c}} - \Delta\varepsilon^T\right)^2 \tag{2}$$

where E_f is the Young's modulus of the fiber and $\Delta\varepsilon^T$ is the difference in thermal expansion between fiber and matrix. This can be reorganized to give the initiation strain $\bar{\varepsilon}_\mathrm{i} = \bar{\sigma}_\mathrm{i}/E_\mathrm{c}$ as:

$$\bar{\varepsilon}_\mathrm{i} = \sqrt{\frac{4G_c}{E_\mathrm{f} r}} + \Delta\varepsilon^T \tag{3}$$

Sørensen [19] shows how τ, G_c and $\Delta\varepsilon^T$ can be determined from the test with this model if measurements of debond length and fiber crack opening as function of load are made. If no crack opening data is available, other measurements on thermal expansion of matrix and fiber can be used to determine $\Delta\varepsilon^T$, after which G_c and τ can be computed from the crack length evolution.

The relation between debond length and applied strain can be simplified to:

$$l_\mathrm{d} = \frac{E_\mathrm{f} r}{2\tau}\left(\bar{\varepsilon} - \bar{\varepsilon}_\mathrm{i}\right) \tag{4}$$

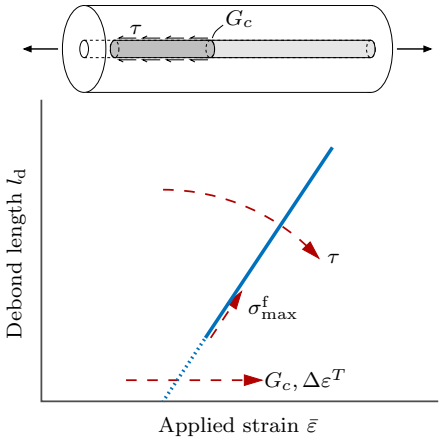

Figure 1: Shear lag theory for single fiber fragmentation test [18, 19], where friction τ influences the slope, fracture energy G_c and residual strain $\Delta\varepsilon^T$ shift the curve and fiber strength $\sigma^\mathrm{f}_\mathrm{max}$ determines how much of the curve needs to be extrapolated to find $\bar{\varepsilon}_\mathrm{i}$.

For a matrix material with hardening nonlinearity, this formulation in terms of applied strain is more suitable than that in terms of $\bar{\sigma}/E_\mathrm{c}$ which assumes linear-elastic behavior. In reality, fiber failure occurs at a strain level that is higher than that needed for onset of debonding, which means that extrapolation is necessary to identify $\bar{\varepsilon}_i$. The influence of the different material properties on the relation between debond length and applied strain is summarized in Figure 1.

For micromechanical modeling of failure in composite materials, the method of choice for modeling fiber/matrix debonding is the cohesive zone method. Therefore, it is of interest to evaluate which cohesive zone properties can be identified with the SFFT. The cohesive zone is located in the fracture process zone where the fracture energy G_c is dissipated. In the context of the shear lag theory (see Fig. 1) this fracture process zone has infinitesimal size, being located in a circumferential line that separates the intact part of the interface from the part where the frictional stress is active. The frictional stress τ that can be measured from the SFFT is therefore not the cohesive shear strength. This frictional stress acts on the cracked surface, where cohesive damage is already equal to 1. The only cohesive property that can be derived from the test according to shear lag theory is the fracture energy.

3. Model description

Two different models are used in this paper to analyse the SFFT setup. Details of both will be presented in this section. Firstly, an axisymmetric model is described for detailed investigation of friction on the debonded fiber. Secondly, a model with a one-dimensional fiber is formulated to analyze the progressive failure and possible interaction between different fiber breaks. The 1D fiber in the second model does not capture possible radial compressive stress acting on the fiber. Therefore a constant frictional stress must be supposed there as a material parameter. The main purpose of the first model is to validate the assumption of constant frictional stress.

3.1. Axisymmetric model

The first model is a standard axisymmetric finite element model. The fiber is modeled with axisymmetric quadrilateral elements close to the axis of symmetry. A cylinder of surrounding matrix material is modeled with triangular axisymmetric elements that increase in size for increasing distance to the fiber. Interface elements with cohesive law are included to model fiber/matrix debonding. A single fiber crack is present at one end of the domain, which is modeled by applying symmetry boundary conditions along that edge only on the nodes associated with the matrix (see Fig. 2). A constant displacement is applied on the far end of the model. This means that the model represents a scenario with distributed fiber breaks at a constant spacing of $2L$.

For the matrix, the pressure-dependent plasticity model by Melro et al. [21] as adapted by Van der Meer [22] is used to describe the nonlinear behavior. The yield surface is given by

$$f = 6J_2 + 2I_1(\sigma_\mathrm{c} - \sigma_\mathrm{t}) - 2\sigma_\mathrm{c}\sigma_\mathrm{t} = 0 \tag{5}$$

Where I_1 is the first invariant of the stress tensor and J_2 is the second invariant of the deviatoric part of the stress tensor and σ_t and σ_c are the tensile and compressive yield stress respectively. Both yield stresses are a function of equivalent

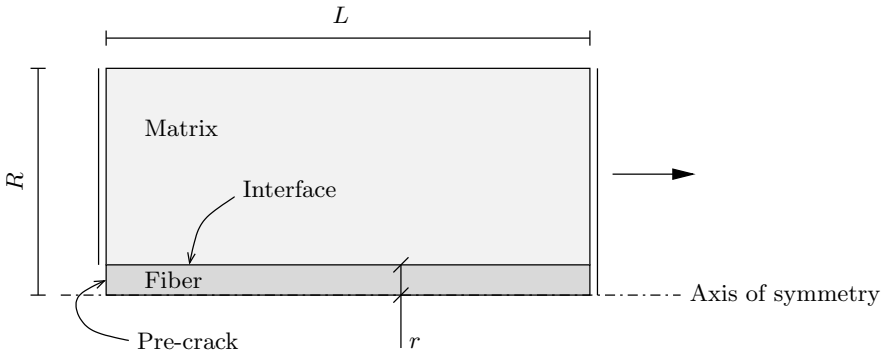

Figure 2: Geometry and boundary conditions of axisymmetric model

plastic strain $\varepsilon_{\mathrm{eq}}^{\mathrm{p}}$, such that measured stress/strain curves from uniaxial tension and uniaxial compression tests can serve as input for the model.

For the fiber-matrix interface, a new cohesive law with friction is used. The formulation by Van der Meer and Sluys [23] based on the cohesive law by Turon et al. [24] and friction according to Alfano and Sacco [25] has been adapted following Zou and Hameed [26].

The traction is defined as

$$\mathbf{t} = (1-d)K\boldsymbol{\delta} + D\mathbf{t}^{\mathrm{fric}} \tag{6}$$

where K is the initial stiffness of the interface, $\boldsymbol{\delta}$ is the displacement jump, $\mathbf{t}^{\mathrm{fric}}$ is the Coulomb frictional traction and d and D are two different representations of the damage variable. The first stands for the relative loss in stiffness and the second for the relative energy dissipation. During the damaging process, they are defined as:

$$D = \frac{\delta_{\mathrm{eq}} - \delta^0}{\delta^f - \delta^0} \tag{7}$$

and

$$d = \frac{\delta^f \left(\delta_{\mathrm{eq}} - \delta^0\right)}{\delta_{\mathrm{eq}} \left(\delta^f - \delta^0\right)} \tag{8}$$

where δ_{eq} is the equivalent displacement jump, and δ^0 and δ^f define the bilinear traction-separation law for the current mode mixity (cf. [24, 27]).

To account for unloading and irreversibility, D is defined as the maximum history value of the right hand side of Eq. (7) and d related to D through

$$d = \frac{D\delta^f}{\delta^0 - D\left(\delta^f - \delta^0\right)} \tag{9}$$

In Eq. (6), $(1-d)K\boldsymbol{\delta}$ is the traction as computed by the frictionless cohesive law, and $D\mathbf{t}^{\text{fric}}$ is the frictional traction that is gradually introduced as damage develops.

The advantage of the approach by Zou and Hameed [26] with D in the second term of Eq. (6) rather than that by Alfano and Sacco [23, 25] which has d in that position, is that it makes the frictional behavior independent of the unphysical K parameter [26].

Zou and Hameed used the friction formulation in combination with a cohesive law with incremental damage update. Here, the decohesion/friction interaction as proposed in Eq. (6) is used in combination with a closed form cohesive law. For consistent linearization of the new cohesive law, expressions are needed for $\partial d/\partial\boldsymbol{\delta}$ as well as for $\partial D/\partial\boldsymbol{\delta}$. Van der Meer et al. [27] have given the consistent expression for $\partial d/\partial\boldsymbol{\delta}$ during damage growth. The one for $\partial D/\partial\boldsymbol{\delta}$ is defined along similar lines as:

$$\frac{\partial D}{\partial\boldsymbol{\delta}} = \frac{\partial D}{\partial\delta_{\text{eq}}}\frac{\partial\delta_{\text{eq}}}{\partial\boldsymbol{\delta}} + \frac{\partial D}{\partial\delta^0_{\text{eq}}}\frac{\partial\delta^0_{\text{eq}}}{\partial\boldsymbol{\delta}} + \frac{\partial D}{\partial\delta^f_{\text{eq}}}\frac{\partial\delta^f_{\text{eq}}}{\partial\boldsymbol{\delta}} \tag{10}$$

3.2. Model with 1D fiber

For analysis of the complete single fiber fragmentation test, it is desirable to eliminate the length scale of the fiber diameter to make the model lighter. Therefore, a formulation with an embedded one-dimensional fiber has been developed. The two or three-dimensional bulk domain must be meshed with solid elements and the fiber with 1D elements. Methods for embedding a fiber in a non-conforming discretization of the bulk exist [28–30], which is a desirable when many fibers are present and meshing all fibers becomes burdensome. However, in the current case of interest with a single fiber, generating a conforming mesh for the bulk that has nodes along the fiber, is not particularly demanding. An

additional advantage of having an element edge coinciding with the fiber is that the stress discontinuity across the fiber, as expected in the shear lag solution, can be captured. An embedded fiber formulation with non-conforming mesh needs a very fine mesh to approximate this stress discontinuity with reasonable accuracy. Therefore, a conforming mesh is used for this study.

The basic kinematic requirement is that slip of the fiber should be supported, i.e. the fiber must be allowed to move in longitudinal direction independently from the surrounding matrix. This could be achieved with bar or truss elements defined on duplicated nodes. However, when duplicated nodes are used, relative displacement of the fiber with respect to the surrounding bulk in transverse direction is also supported, which must be constrained or penalized. A more elegant solution is to define a model where already in the kinematic formulation the only supported relative movement of the fiber is movement in longitudinal direction.

Here, this is achieved by introducing slip degrees of freedom on the nodes where the fiber is positioned (see Figure 3). The starting point is a standard displacement field for the matrix $\mathbf{u}^{\mathrm{m}}$. The strain in the matrix is defined as

$$\boldsymbol{\varepsilon}^{\mathrm{m}} = \nabla^{\mathrm{s}} \mathbf{u}^{\mathrm{m}} \tag{11}$$

On the location of the fiber, an additional one-dimensional unknown field Δ^{fm} is defined that represents the amount of slip. The displacement of the fiber is then defined as the sum of the two fields:

$$\mathbf{u}^{\mathrm{f}}(x, y) = \mathbf{u}^{\mathrm{m}}(x, y) + \Delta^{\mathrm{fm}}(\zeta)\boldsymbol{\zeta} \tag{12}$$

where ζ is an auxiliary coordinate defined along the fiber. The axial strain of the fiber is:

$$\varepsilon^{\mathrm{f}} = \frac{\partial \mathbf{u}^{\mathrm{f}} \cdot \boldsymbol{\zeta}}{\partial \zeta} = \frac{\partial \mathbf{u}^{\mathrm{m}} \cdot \boldsymbol{\zeta}}{\partial \zeta} + \frac{\partial \Delta^{\mathrm{fm}}}{\partial \zeta} \tag{13}$$

The fiber is connected to the surrounding bulk with cohesive and frictional tractions. The virtual work equation for this problem is given as:

$$\int_{\Omega} \delta\boldsymbol{\varepsilon}^{\mathrm{m}} : \boldsymbol{\sigma}^{\mathrm{m}} \, \mathrm{d}\Omega + \int_{\Gamma^{\mathrm{f}}} \left(A^{\mathrm{f}} \delta\varepsilon^{\mathrm{f}} \sigma^{\mathrm{f}} + C^{\mathrm{f}} \delta\Delta^{\mathrm{fm}} t \right) \mathrm{d}\Gamma = \int_{\Gamma^{N}} \delta\mathbf{u} \cdot \mathbf{t}^{N} \, \mathrm{d}\Gamma \tag{14}$$

where Ω is the matrix domain, Γ^{f} is the one dimensional fiber domain, A^{f} and C^{f} are the area and circumference of the fiber cross section respectively, t is the cohesive and/or frictional sliding traction acting on the fiber/matrix interface and $\mathbf{t}^N$ is the external traction applied on Γ^N.

The matrix displacement field is discretized with two or three-dimensional shape functions $\phi(\mathbf{x})$:

$$\mathbf{u}^{\mathrm{m}}(\mathbf{x}) = \phi_i(\mathbf{x})\hat{\mathbf{u}}_i^{\mathrm{m}}, \quad i \in [1, nn^{\Omega}] \tag{15}$$

where $\hat{\mathbf{u}}_i$ contains the nodal displacements of node i, and nn^{Ω} is the total number of nodes. Summation over repeating index i is implied. The slip field is discretized with one-dimensional shape functions $\psi(\zeta)$:

$$\Delta^{\mathrm{fm}}(\zeta) = \psi_j(\zeta)\hat{\Delta}_j^{\mathrm{fm}}, \quad j \in [1, nn^{\Gamma}] \tag{16}$$

where nn^{Γ} is the number of nodes along the fiber. For the definition of fiber strain in Eq. (13), the projection of the displacement vector $\mathbf{u}^{\mathrm{f}}$ in $\boldsymbol{\zeta}$ direction is needed. As long as the order of interpolation $\psi(\zeta)$ is equal to that of $\phi(\mathbf{x})$, we have $\psi_j(\zeta) = \phi_{i(j)}(\mathbf{x}(\zeta))\ \forall\ \zeta \in \Gamma^{\mathrm{f}}$ where the subscript $i(j)$ refers to a map that returns the global node index $i \in [1, nn^{\Omega}]$ for a given fiber node index $j \in [1, nn^{\Gamma}]$. Therefore, we can write:

$$\mathbf{u}^f(\zeta) \cdot \boldsymbol{\zeta} = \psi_j(\zeta)\left(\hat{\mathbf{u}}_{i(j)}^{\mathrm{m}} \cdot \boldsymbol{\zeta} + \hat{\Delta}_j^{\mathrm{fm}}\right), \quad j \in [1, nn^{\Gamma}] \tag{17}$$

With this discretization the virtual work equation from Eq. (14) can be written as the following set of equations:

$$\begin{Bmatrix} \mathbf{f}_u^{\mathrm{int}} \\ \mathbf{f}_{\Delta}^{\mathrm{int}} \end{Bmatrix} = \begin{Bmatrix} \mathbf{f}_u^{\mathrm{ext}} \\ 0 \end{Bmatrix} \tag{18}$$

with:

$$\mathbf{f}_u^{\mathrm{int}} = \int_{\Omega} \mathbf{B}^T \boldsymbol{\sigma}^{\mathrm{m}}\, \mathrm{d}\Omega + \int_{\Gamma^{\mathrm{f}}} \mathbf{B}_{u\zeta}^T \sigma^{\mathrm{f}} A^{\mathrm{f}}\, \mathrm{d}\Gamma \tag{19}$$

$$\mathbf{f}_u^{\mathrm{ext}} = \int_{\Gamma^N} \mathbf{N}^T \mathbf{t}\, \mathrm{d}\Gamma \tag{20}$$

$$\mathbf{f}_{\Delta}^{\mathrm{int}} = \int_{\Gamma^{\mathrm{f}}} \nabla \boldsymbol{\psi}^T \sigma^{\mathrm{f}} A^{\mathrm{f}}\, \mathrm{d}\Gamma + \int_{\Gamma^{\mathrm{f}}} \boldsymbol{\psi}^T t C^{\mathrm{f}}\, \mathrm{d}\Gamma \tag{21}$$

where $\mathbf{B}$ and $\mathbf{N}$ are the standard finite element strain-displacement matrix and shape function matrix, while $\mathbf{B}_{u\zeta}$ is a vector that contains for every node i the product of the 1D shape function gradient in fiber direction and the fiber direction vector:

$$(\mathbf{B}_{u\zeta})_i = \frac{\partial \psi_i}{\partial \zeta}\boldsymbol{\zeta} \tag{22}$$

Linearization of this system of equations gives the following stiffness matrix:

$$\mathbf{K} = \begin{bmatrix} \mathbf{K}_{uu} & \mathbf{K}_{u\Delta} \\ \mathbf{K}_{\Delta u} & \mathbf{K}_{\Delta\Delta} \end{bmatrix} \tag{23}$$

with

$$\begin{aligned} \mathbf{K}_{uu} &= \int_\Omega \mathbf{B}^T \mathbf{D} \mathbf{B} \,\mathrm{d}\Omega + \int_{\Gamma^\mathrm{f}} \mathbf{B}_{u\zeta}^T D^\mathrm{f} \mathbf{B}_{u\zeta} \,\mathrm{d}\Gamma \\ \mathbf{K}_{u\Delta} &= \int_{\Gamma^\mathrm{f}} \mathbf{B}_{u\zeta}^T D^\mathrm{f} \nabla\boldsymbol{\psi} \,\mathrm{d}\Gamma \\ \mathbf{K}_{\Delta u} &= \int_{\Gamma^\mathrm{f}} (\nabla\boldsymbol{\psi})^T D^\mathrm{f} \mathbf{B}_{u\zeta} \,\mathrm{d}\Gamma \\ \mathbf{K}_{\Delta\Delta} &= \int_{\Gamma^\mathrm{f}} \left((\nabla\boldsymbol{\psi})^T D^\mathrm{f} \nabla\boldsymbol{\psi} + \boldsymbol{\psi}^T D^t \boldsymbol{\psi} \right) \mathrm{d}\Gamma \end{aligned} \tag{24}$$

and

$$\begin{aligned} \mathbf{D} &= \frac{\partial \boldsymbol{\sigma}^\mathrm{m}}{\partial \boldsymbol{\varepsilon}^\mathrm{m}} \\ D^\mathrm{f} &= A^\mathrm{f} \frac{\partial \sigma^\mathrm{f}}{\partial \varepsilon^\mathrm{f}} \\ D^t &= C^\mathrm{f} \frac{\partial t}{\partial \Delta^\mathrm{fm}} \end{aligned} \tag{25}$$

For the matrix stress $\boldsymbol{\sigma}^\mathrm{m}$, Melro's plasticity model as described in the previous section is used. For the fiber/matrix slip, a one-dimensional version of the bilinear cohesive law with friction is used. This is the pure mode II version of the mixed mode cohesive law described in the previous section. Because of the 1D nature of the fiber, no pressure on the interface is computed. Therefore, the frictional stress is assumed to be constant, instead of a product of the friction coefficient and the normal pressure. Again following Zou and Hameed [26] the 1D cohesive law is formulated such that the traction decreases linearly from its maximum value to the constant friction value. Because the frictional value is

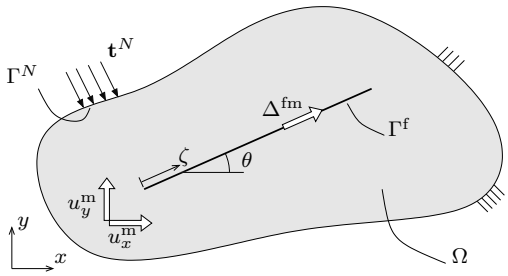

Figure 3: Definition of coordinates x, y and ζ, unknown fields u_x^{m}, u_y^{m} and Δ^{fm} and corresponding domains Ω and Γ^{f}

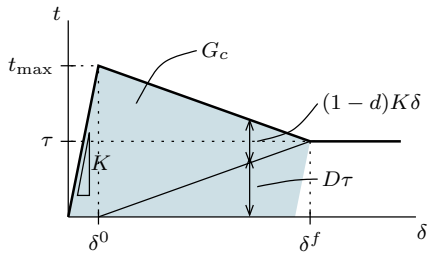

Figure 4: One-dimensional version of Zou and Hameed cohesive law with constant friction and definition of G_c.

given a priori, the fracture energy can be taken to include the frictional traction that is linearly introduced during damage development as shown in Figure 4.

Brittle fiber failure is included in the 1D fiber model. A Weibull strength distribution is used to define the variation of the strength along the fiber. On every node a strength value is assigned. Following Nishikawa et al. [10], a Weibull distribution is achieved by computing nodal strength values as:

$$\sigma^{\mathrm{f}}_{\max,i} = \sigma^{\mathrm{f}}_{\max,0} \left(-\frac{l_0}{\Delta l} \log(1-\phi_i) \right)^{1/\rho} \tag{26}$$

where $\sigma^{\mathrm{f}}_{\max,0}$ is the reference strength for a fiber of length l_0, Δl is the element size, ϕ_i is a random number from a uniform distribution and ρ is the Weibull modulus. In the simulations, after equilibrium is reached, the nodal stress in the fiber is compared to the local strength value $\sigma^{\mathrm{f}}_{\max,i}$. If the stress is higher then the strength, the fiber breaks, which is achieved by duplicating the slip degree of freedom on the associated node and redefining the degree of freedom table of

neighboring elements such that they do not share a slip dof.

The fiber is allowed to break at only one location at a time: the location where the ratio of stress over strength has the highest value. After fiber failure, the Newton-Raphson iterative procedure for the same time step is continued to find the equilibrium solution for the updated discretization, and after convergence, fiber failure is checked for again. The next time step is entered only after an equilibrium solution is found for which the stress in the fiber does not exceed the strength at any point.

When realistic parameters are used for fiber and fiber/matrix interface, unstable propagation of debonding over a finite length is possible. For this reason, the Newton-Raphson procedure sometimes has difficulties converging after fiber failure. When non-convergence after fiber failure is encountered, a sub-stepping is introduced to gradually go through the unstable propagation. A traction is introduced that acts against separation between the two slip dofs on the same node. This traction is removed is steps of 0.5^n where n is the substep level. Every time the solution does not converge, n is increased with 1. This is continued until the traction is completely removed. The whole procedure is performed at fixed applied displacement level within a single time step. This means that no spurious tractions across the fiber break are present in the final solution for any time step.

4. Results

4.1. Axisymmetric analysis

A single fiber fragmentation test with glass fiber in epoxy matrix is simulated. The fiber has a radius of $r = 7.5\,\mu$m. Material properties for the fiber/matrix interface are estimated. Fiber and matrix parameters are taken as determined from own experiments on glass fibers and epoxy [31]. The elastic behavior of the fibers is given by $E^{\mathrm{f}} = 73\,\mathrm{GPa}$ and $\nu^{\mathrm{f}} = 0.22$, that of the matrix by $E^{\mathrm{m}} = 3.13\,\mathrm{GPa}$ and $\nu^{\mathrm{m}} = 0.37$. The fitted hardening curves (in MPa) are

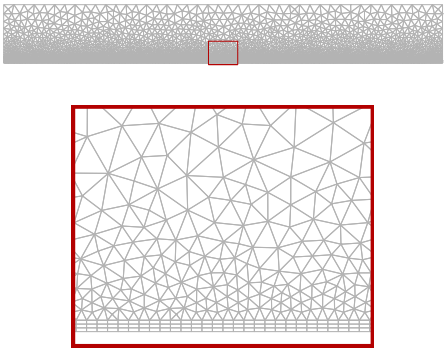

Figure 5: Mesh for axisymmetric model.

given by:

$$\begin{aligned} \sigma_{\mathrm{t}} &= 71.3997 - 34.1296e^{-\varepsilon^{\mathrm{p}}_{\mathrm{eq}}/0.0057} - 14.8590e^{-\varepsilon^{\mathrm{p}}_{\mathrm{eq}}/0.0012} \\ \sigma_{\mathrm{c}} &= 89.2022 - 24.1071e^{-\varepsilon^{\mathrm{p}}_{\mathrm{eq}}/0.0097} - 10.4262e^{-\varepsilon^{\mathrm{p}}_{\mathrm{eq}}/0.0016} \end{aligned} \tag{27}$$

For the cohesive law, the strength for both normal and shear loading is set to 40 MPa. Furthermore, for the fracture energy, we use $G_{Ic} = 0.02\,\mathrm{N/mm}$ and $G_{IIc} = 0.05\,\mathrm{N/mm}$, with mode interaction parameter $\eta = 1$. The friction coefficient is $\mu = 0.3$. Residual stresses are included with coefficients of thermal expansion for fiber and matrix of $\alpha^{\mathrm{f}} = 5.4 \cdot 10^{-6}\,\mathrm{K}^{-1}$ and $\alpha^{\mathrm{m}} = 60 \cdot 10^{-6}\,\mathrm{K}^{-1}$ and an assumed temperature drop after curing of $\Delta T = -27$ K.

The axisymmetric model is analyzed with $L = 3\,\mathrm{mm}$, while the outer radius R is varied from 0.4 mm to 0.8 mm and 1.6 mm. The mesh for $R = 0.4\,\mathrm{mm}$ is shown in Figure 5. In Figure 6 the evolution of crack length as a function of applied strain is shown, along with the theoretical result from Eq. (4) with a fitting value for the interfacial traction of $\tau = 5\,\mathrm{MPa}$. For the case of an elastic matrix, the radius of the domain does not influence the results. When plasticity is included, it only influences the level at which the debond stops growing. The debond arrest is caused by the formation of a perfectly plastic region. As a consequence of the plastic mechanism, the strain in the matrix is no longer uniform; the strain only increases in the region near the plane of symmetry. It is observed that when plasticity is included, the crack length follows the linear

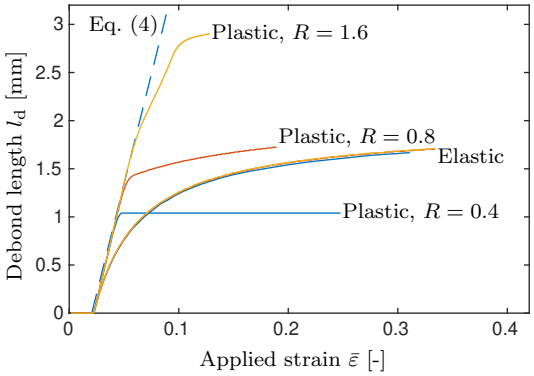

Figure 6: Development of debond length in axisymmetric model with or without plastic matrix behavior and different domain sizes, in comparison with reference solution from Eq. (4) with $\tau = 5\,\mathrm{MPa}$ (dashed line). Note that the elastic curve is not significantly affected by changing R.

function of applied strain, as long as no plastic mechanism forms. Without plasticity, the trend is different and the linear relation between l_d and $\bar{\varepsilon}$ from theory is not recovered.

To explain the cause for the difference, the traction along the fiber matrix interface is shown for three different time steps in Figure 7 (with $R = 0.8\,\mathrm{mm}$). The curves show a clear peak in the stress indicating the position of the crack tip. The ascending part of the curve on the left side of the peak is where the cohesive zone is located. As the crack grows, the cohesive zone shifts to the right, without changing size. It can be observed that in the case with linear elastic matrix, the traction along the fully damaged part (i.e. on the left side of the cohesive zone) increases, while it remains approximately constant in the case with an elastic/plastic matrix. It is concluded that the constant traction assumption from the shear lag theory is justified, but only if matrix plasticity is present. The value of $\tau = 5\,\mathrm{MPa}$ that gave a good fit for the reference solution in Fig. 6 is visualized with the dashed line in Fig. 7. The fact that the friction in the model is indeed at this level confirms the agreement between the assumptions behind the theory and the processes predicted by the model.

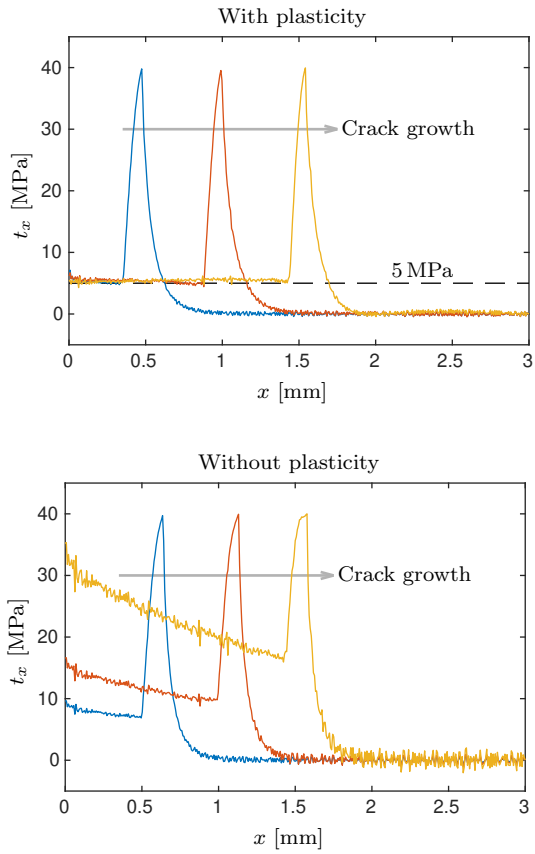

Figure 7: Shear component of cohesive traction for three different time steps from simulations with and without plasticity in the matrix.

4.2. Progressive failure analysis with 1D fiber

The axisymmetric results show that, as a consequence of matrix plasticity, a constant frictional stress is a reasonable assumption. To investigate the assumption that there is no interaction between different fragments until saturation, the model with embedded 1D fiber is used. The same parameters are used as in the axisymmetric analysis, except for the following. The cohesive zone now only receives mode II properties. The element size along the fiber is $\Delta l = 0.005\,\text{mm}$. Thermal contraction is left out of consideration. In order to stop debonding from growing too fast, the frictional stress is set to $\tau = 30\,\text{MPa}$ and the cohesive strength to $t_{\max} = 50\,\text{MPa}$. Additionally, the following parameters are used

for the fiber failure: $\sigma^{\mathrm{f}}_{\mathrm{max},0} = 2000\,\mathrm{MPa}$, $l_0 = 10\,\mathrm{mm}$, $\rho = 5$.

Again, the simulation is performed with and without plasticity. Just like in the test, multiple fiber breaks occur sequentially as the load is increased. The individual debond lengths surrounding each of these breaks are monitored during the simulation. Figure 8 shows the progression of different quantities by plotting for different time steps the equivalent plastic strain in the matrix, the stress in the fiber and the traction along the fiber/matrix interface (all quantities are normalized, the figure is intended as a qualitative illustration of the sequence of events). Fiber breaks are located where the fiber stress is equal to zero. Regions with constant nonzero traction indicate the fully damaged areas where the frictional stress is fully introduced. The plastic strain field shows the shear bands under $\pm 45^\circ$ angle as can also be observed in the polarized light images (see Fig. 9). These cannot be observed in any of the stress or strain fields when the matrix is taken to be elastic. It is concluded that the visible shear bands in the experiment are also caused by large scale plasticity.

Figure 10 shows the evolution of the debond length for the simulations with and without plasticity in the matrix. Every dot represents the total debond length ($2l_{\mathrm{d}}$) around a single fiber break for a single time step. The debond length as predicted by shear lag theory is also shown in the figures. It is observed that the debond length evolution in the computational model agrees well with theory. Unlike with the axisymmetric model, the simulations without plasticity here also agree with theory. This is due to the assumption of constant friction, which is made here, even though the axisymmetric simulations did not show this.

The debond length of different cracks is equal until they are arrested when approaching each other. In both simulations, two debonds appear at an applied strain between 0.03 and 0.04 for which the length is smaller than that of other debonds. These correspond to two fiber breaks that are so close that they immediately feel each other. In the simulation with plasticity, the debond length development halts for almost all cracks when a plastic mechanism forms. The strain distribution becomes non-uniform in a global sense and the assumption

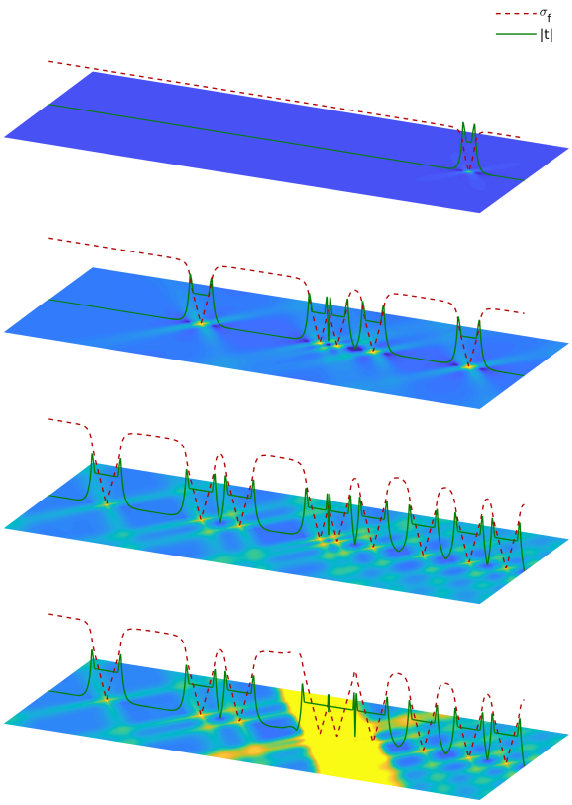

Figure 8: Fiber stress, interfacial traction and equivalent plastic strain for four different time steps.

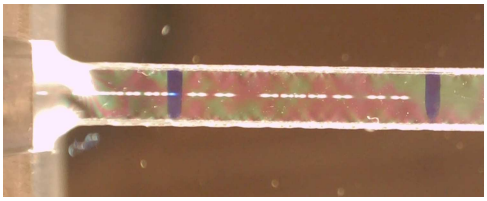

Figure 9: Experimental image showing fiber matrix debonding at several locations and shear bands emanating from those locations.

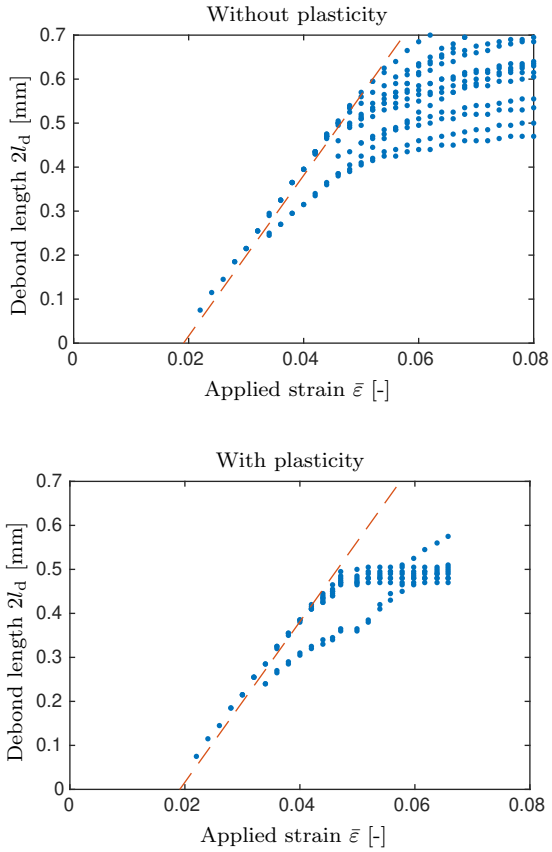

Figure 10: Development of debond length as function of applied strain in comparison with shear lag theory (Eq. (4)).

that the strain in bonded parts of the fiber is equal to the globally applied strain $\bar{\varepsilon}$ loses validity.

It is concluded that shear lag theory holds also when multiple fiber breaks are present. Until onset of strain localization, the debond length development is the same for the simulations with and without plasticity. The shear bands that are observable in experiments and in the simulation with plasticity, but not in the simulation without plasticity, do therefore not influence the debond length development.

This simulation illustrates that, with shear lag theory, no saturation of fiber fragmentation is needed before useful information can be extracted from the test.

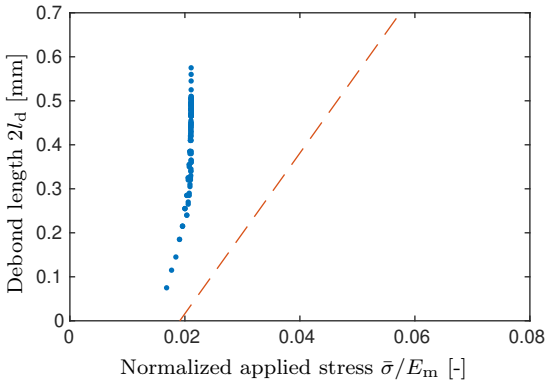

Figure 11: Development of debond length as function of applied stress in comparison with shear lag theory [19].

Early interpretations of the test were based on observations of when saturation takes place. Matrix failure prior to saturation, as happens in this simulation, would invalidate the test. However in this virtual test, both τ and G_c could be determined from looking at the debond length development, even though saturation is not reached.

In Figure 11, the results from the simulation with plasticity are visualized once more, but now with the applied stress divided by initial stiffness along the horizontal axis, instead of the applied strain. This is the representation that Sørensen uses in his expressions [19] (cf. Eq. (1)). In this visualization the apparent agreement between theory and numerical results is much less than it was in Fig. 10. The important quantity in the shear lag theory is the fiber strain. By design of the specimen, the fiber strain is equal to the overall applied strain, while for a matrix material showing significant nonlinearity as the one used in this study the fiber strain does not remain proportional to the applied stress.

4.3. Cohesive zone length study with 1D fiber

The SFFT has been proposed as a test with which the interfacial strength can be measured. In the original interpretation of the test, this strength is equivalent to the frictional stress in the simulations in this paper. The magnitude of this frictional stress can indeed be identified from this test, but it is not the same

thing as the interfacial strength. Sørensen's shear lag model is a linear elastic fracture mechanics model with infinitely small fracture process zone, which implies the presence of a stress singularity. The models from the present paper include a cohesive zone with a cohesive strength. This cohesive strength is what is needed for multiscale or micromechanical modeling of failure of composite materials; it is emphasized here that the cohesive strength is not something that can be directly measured in the SFFT.

Nevertheless, there is a way to get indirect information on the cohesive strength. It is known that the cohesive zone length is a function of, among other quantities, the cohesive strength [32, 33]. This also holds for the SFFT. Having learnt that in the 1D fiber model there is no influence of plasticity or interaction between debond zones, the simulations with embedded fiber are repeated with a single fiber break and an elastic matrix. A series of simulations is performed varying the cohesive strength from 50 MPa to 100 MPa. In every simulation, the length of the two cohesive zones (on either side of the fiber break) has been monitored. This length was constant throughout the simulation, apart from minor oscillations. Averaging the cohesive zone length over all time steps in which complete cohesive zones were present leads to a single value of the cohesive zone length per simulation. In Figure 12, these values are plotted as function of the input cohesive strength, along with an analytical curve of the shape

$$l_{\mathrm{cz}}^{\mathrm{ana}} = \frac{50 l_{\mathrm{cz}}^{50}}{t_{\max}} \tag{28}$$

where l_{cz}^{50} is the cohesive zone length found for $t_{\max} = 50\,\mathrm{MPa}$. It can be concluded that there is a clear dependence of cohesive zone length on the cohesive strength and that this dependence seems to be of the order $t_{\max}^{-1}$.

In the experiments, a fracture process zone near the tip of the fiber/matrix debond region is visible along with a stress concentration. The shape of the zone is similar to what is observed in the embedded fiber simulations. A rough estimate of the cohesive strength can therefore be obtained by changing the input cohesive strength such that the fracture process zone size in the simulations

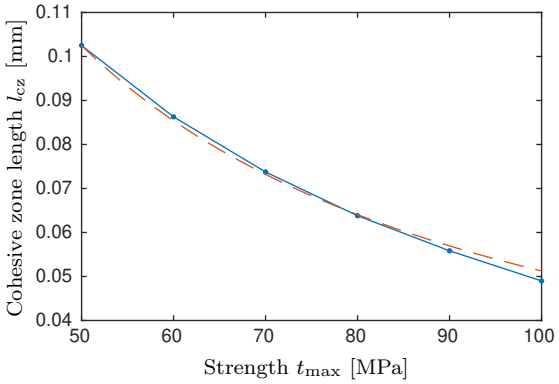

Figure 12: Cohesive zone length for different values of the strength; dashed line represents $l_{\mathrm{cz}}^{\mathrm{ana}}$ from Eq. (28).

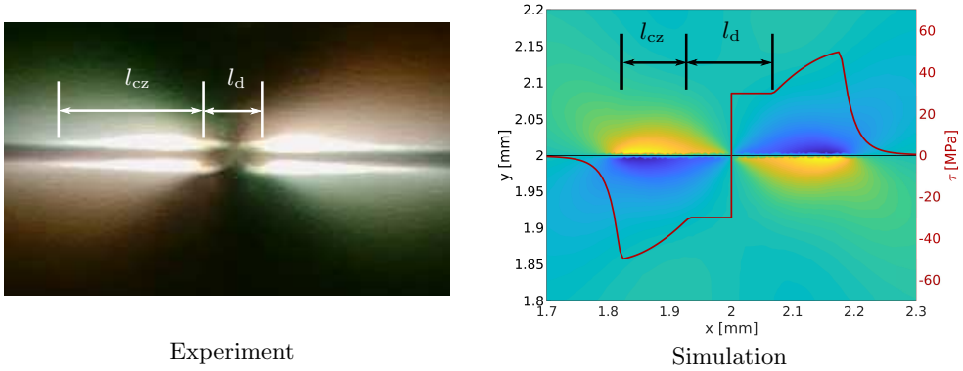

Figure 13: Comparison between debond length and cohesive zone length in experimental observations and simulation results indicating shear stress (shading) and traction (solid line).

matches the experimental observations (see Fig. 13). Another influence on the cohesive zone size is the shape of the traction-separation law. Therefore, it cannot be concluded that the thus obtained value for the cohesive strength is equal to the actual maximum traction that is present along the interface in the test. Nevertheless, this recipe leads to the value for the cohesive strength which, for the assumed cohesive zone shape, leads to the closest match with experimental observations of the fracture process zone. We have used this procedure in [34] to estimate the degradation of interfacial strength due to hygrothermal aging.

A further parametric study has shown that the cohesive zone length is also dependent on the fiber diameter, the frictional stress and the fracture energy. Therefore, it is important that these are all characterized first before the cohesive strength is estimated from the proposed inverse modeling exercise. Fortunately, both can be identified from debond length measurements in the SFFT using the now validated shear lag approach.

5. Conclusions

The presented numerical investigation into the SFFT has led to the confirmation of the previously hypothesized shear lag theory. Firstly, the assumption of a constant frictional stress on the debonded fiber/matrix interface is confirmed by the simulations, but only in presence of plasticity in the surrounding bulk material. Secondly, the assumption that there is no interaction between different debond zones has been validated. Even though there is large scale plasticity with global shear bands, the matrix deformations that are not accounted for in shear lag theory do not influence the debond process significantly. However, in presence of nonlinearity, it is important that applied strain is monitored rather than the applied stress.

New modeling ingredients have been introduced. The cohesive law that combines decohesion with friction without spurious influence of initial stiffness with a newly derived consistent tangent has been proven to be robust. The finite element framework with embedded fiber in conforming mesh with slip degrees of freedom on the fiber domain is a robust and efficient tool for analysis of fracture and debonding of isolated fibers in a bulk material.

Moreover, recommendations for the interpretation of the test have been made. Firstly, it is recommended to analyze the debond length as a function of applied strain rather than of applied stress. For nonlinear materials this makes a significant difference. Secondly, it is highlighted that it is possible to use inverse modeling to get information on the cohesive shear strength of the fiber/matrix interface.

Acknowledgment

This work was supported by the Netherlands Enterprise Agency (RVO) under TKI-WoZ project MIMIC (TKIW02005).

Declaration of interest

Declarations of interest: none.

Data availability

Data presented in this article are available at the 4TU.ResearchData repository through http://doi.org/10.4121/uuid:5d4e90c2-905e-432b-bf30-abd146518370

References

References

[1] A Kelly and WR Tyson. Tensile properties of fibre-reinforced metals: Copper/tungsten and copper/molybdenum. *J Mech Phy Solids*, 13:329–350, 1965.

[2] A Awal, G Cescutti, SB Ghosh, and J Müssig. Interfacial studies of natural fibre/polypropylene composites using single fibre fragmentation test (SFFT). *Compos Part A*, 42:50–56, 2011.

[3] R Joffe, J Andersons, and Wallström. Strength and adhesion characteristics of elementary flax fibres with different surface treatments. *Compos Part A*, 34:603–612, 2003.

[4] JR Wood and G Marom. Determining the interfacial shear strength in the presence of transcrystallinity in composites by the 'single-fibre microcomposite compressive fragmentation test'. *Appl Compos Mater*, 4:197–207, 1997.

[5] CL Schutte, W McDonough, M Shioya, and M McAuliffe. The use of the single-fibre fragmentation test to study the environmental durability of interfaces/interphases between DGEBA/mPDA epoxy and glass fibre: The effect of moisture. *Compos*, 25:617–624, 1994.

[6] BW Kim and JA Nairn. Observations of fiber fracture and interfacial debonding phenomena using the fragmentation test in single fiber composites. *J Compos Mater*, 36:1825–1858, 2002.

[7] C Galiotis. A study of mechanism of stress transfer in continuous- and discontinuous model composite by laser Raman spectroscopy. *Compos Sci Technol*, 48:15–28, 1993.

[8] D Tripathi and FR Jones. Measurement of the load-bearing capability of the fibre/matrix interface by single-fibre fragmentation. *Compos Sci Technol*, 57:925–935, 1997.

[9] D Tripathi and FR Jones. Single fibre fragmentation test for assessing adhesion in fibre reinforced composites. *J Mater Sci*, 33:1–16, 1998.

[10] M Nishikawa, T Okabe, N Takeda, and W Curtin. Micromechanics of the fragmentation process in single-fiber composites. *Modell Simul Mat Sci Eng*, 16:1–19, 2008.

[11] E Graciani, V Mantič, F París, and J Varna. Numerical analysis of debond propagation in the single fibre fragmentation test. *Compos Sci Technol*, 69:2514–2520, 2009.

[12] JA Nairn and YC Liu. Stress transfer into a fragmented anisotropic fiber through an imperfect interface. *Int J Solids Struct*, 34:1255–1281, 1997.

[13] BW Kim and JA Nairn. Experimental verification of the effects of friction and residual stress on the analysis of interfacial debonding and toughness in single fiber composites. *J Mater Sci*, 37:3965–3972, 2002.

[14] D Tripathi, F Chen, and FR Jones. The effect of matrix plasticity on the stress fields in a single filament composite and the value of interfacial shear strength obtained from the fragmentation test. *Proc R Soc London A*, 452:621–653, 1996.

[15] AC Johnson, SA Hayes, and FR Jones. Data reduction methodologies for single fibre fragmentation test: Role of the interface and interphase. *Compos Part A*, 40:449–454, 2009.

[16] W Wu, I Verpoest, and J Varna. Prediction of energy release rate due to the growth of an interface crack by variational analysis. *Compos Sci Technol*, 60:351–360, 2000.

[17] JW Hutchinson and HM Jensen. Models of fiber debonding and pullout in brittle composites with friction. *Mech Mater*, 9:139–163, 1990.

[18] BF Sørensen and H Lilholt. Fiber pull-out test and single fiber fragmentation test - analysis and modelling. *IOP Conf Series: Materials Science and Engineering*, 139, 2016.

[19] BF Sørensen. Micromechanical model of the single fiber fragmentation test. *Mech Mater*, 104:38–48, 2017.

[20] J Varna, R Joffe, and LA Berglund. Interfacial toughness evaluation from the single-fiber fragmentation test. *Compos Sci Technol*, 56:1105–1109, 1996.

[21] AR Melro, PP Camanho, FM Andrade Pires, and ST Pinho. Micromechanical analysis of polymer composites reinforced by unidirectional fibres: Part I - Constitutive modelling. *Int J Solids Struct*, 50:1897–1905, 2013.

[22] FP van der Meer. Micromechanical validation of a mesomodel for plasticity in composites. *Eur J Mech Solids*, 60:58–69, 2016.

[23] FP van der Meer and LJ Sluys. A numerical investigation into the size effect in the transverse crack tensile test for mode II delamination. *Compos Part A*, 54:145–152, 2013.

[24] A Turon, PP Camanho, J Costa, and CG Dávila. A damage model for the simulation of delamination in advanced composites under variable-mode loading. *Mech Mater*, 38:1072–1089, 2006.

[25] G Alfano and E Sacco. Combining interface damage and friction in a cohesive-zone model. *Int J Numer Method Eng*, 68:542–582, 2006.

[26] Z Zou and M Hameed. Combining interface damage and friction in cohesive interface models using an energy based approach. *Compos Part A*, 112:290–298, 2018.

[27] FP van der Meer and LJ Sluys. Mesh-independent modeling of both distributed and discrete matrix cracking in interaction with delamination. *Eng Fract Mech*, 77:719–735, 2010.

[28] FKF Radtke, A Simone, and LJ Sluys. A computational model for failure analysis of fibre reinforced concrete with discrete treatment of fibres. *Eng Fract Mech*, 77:597–620, 2010.

[29] VMCF Cunha, JAO Barros, and JM Sena-Cruz. A finite element model with discrete embedded elements for fibre reinforced composites. *Comput Struct*, 94-95:22–33, 2012.

[30] J Kang, K Kim, YM Lim, and JE Bolander. Modeling of fiber-reinforced cement composites: Discrete representation of fiber pullout. *Int J Solids Struct*, 51:1970–1979, 2014.

[31] IBCM Rocha, FP van der Meer, RPL Nijssen, and LJ Sluys. A multiscale and multiphysics numerical framework for modelling of hygrothermal ageing in laminated composites. *Int J Numer Method Eng*, 112:360–379, 2017.

[32] QD Yang and BN Cox. Cohesive models for damage evolution in laminated composites. *Int J Fract*, 133:107–137, 2005.

[33] PW Harper and SR Hallett. Cohesive zone length in numerical simulations of composite delamination. *Eng Fract Mech*, 75:4774–4792, 2008.

[34] IBCM Rocha, FP van der Meer, S Raijmaekers, F Lahuerta, RPL Nijssen, LP Mikkelsen, and LJ Sluys. A combined experimental/numerical investigation on hygrothermal aging of fiber-reinforced composites. *Eur J Mech Solids*, 73:407–419, 2019.